Research Square

Preprints are preliminary reports that have not undergone peer review.
They should not be considered conclusive, used to inform clinical practice,
or referenced by the media as validated information.

Current selects the helicity of a chiral phonon

Swagata Acharya

swagata.acharya@nlr.gov

National Laboratory of the Rockies

Jerome Jackson

Daresbury Laboratory

Mark van Schilfgaarde

National Laboratory of the Rockies

Article

Keywords:

Posted Date: November 9th, 2026

DOI: https://doi.org/10.21203/rs.3.rs-11369791/v1

License: This work is licensed under a Creative Commons Attribution 4.0 International License.
Read Full License

Additional Declarations: No competing interests reported.

Current selects the helicity of a chiral phonon

Swagata Acharya,[1,*] Jerome Jackson,[2] and Mark van Schilfgaarde[1]

[1] *National Laboratory of the Rockies, Golden, Colorado, USA*

[2] *Scientific Computing Department, STFC Daresbury Laboratory, Warrington WA4 4AD, United Kingdom*

Abstract

The emergence of spin-polarized electrons from nonmagnetic chiral molecules and crystals is called Chirality-induced spin selectivity (CISS). A chiral phonon of definite wavevector q can strongly enhance it, but near equilibrium the two helicities $+q$ and $-q$ are equally populated: they are time-reversal partners and their contributions cancel. We show that in a biased chiral conductor the current causes the phonon of one helicity to damp less than the other. The damping asymmetry is odd in the current, odd under $q \to -q$, invariant under a mirror that reverses the structural handedness, and equal, mode for mode, to the current-induced nonconservative Berry force on the phonon coordinate. Closing the phonon kinetics with a rate equation turns the asymmetry into a net lattice helicity: at any finite bias one helicity is preferentially populated, with no threshold, growing linearly with the current as $V \to 0$; above a threshold that helicity becomes a self-sustained coherent travelling wave. We demonstrate this effect in elemental tellurium, treated as an open quantum system (electronic Hamiltonian, phonon bath, and electron–phonon coupling) within a quasi-*ab initio* framework. The electronic Hamiltonian is supplied by a vertex-corrected quasiparticle self-consistent GW (QS$G\hat{W}$) potential with spin–orbit coupling; nuclear displacements are modeled with a machine-learned interatomic potential, which yields chiral phonon modes at finite $\pm q_z$ on the Γ–A line. The perturbation to the electronic Hamiltonian from a nuclear displacement is approximated by a frozen-phonon deformation potential. In tellurium the damping asymmetry grows linearly with the current, the resulting lattice helicity persists from low temperature to room temperature, and the coherent regime appears below about 20 K at 0.2 V and 40 K at 0.4 V. No optical pump is needed: a bias alone drives the current and selects the phonon helicity; reversing the current reverses the selection.

I. INTRODUCTION

Electrons transmitted through a chiral molecule or crystal emerge spin polarized, even though neither the incident electrons nor the material carries a net magnetization. This is called chirality-induced spin selectivity (CISS).[1–8] First observed in simple molecules, it has since been demonstrated across self-assembled monolayers, hybrid perovskites, and

* swagata.acharya@nlr.gov

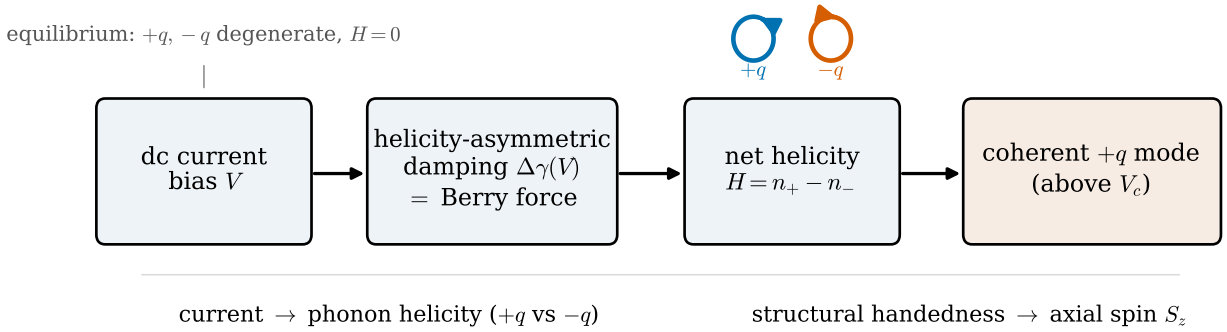


FIG. 1. Selection of a chiral-phonon helicity by a dc current. At equilibrium the $+q$ and $-q$ modes are degenerate time-reversal partners and the net helicity vanishes. A bias drives the electrons into a steady state that damps the two helicities unequally; the asymmetry $\Delta\gamma(V)$ is the same object as a nonconservative Berry force on the phonon coordinate. A phonon rate equation converts $\Delta\gamma$ into a net helicity $H = n_+ - n_-$ at any finite bias, and, above a threshold V_c, into a self-sustained coherent travelling mode of definite q. Structural handedness, through spin–orbit coupling in the electronic Hamiltonian H_0, sets the axial spin S_z that correlates to the selected mode.

layered crystals.[9–12] It now serves as a potential framework for spintronics without ferromagnets and enantioselective enhancement of catalytic and electrochemical reactions. Its microscopic origin, however, remains an open question. Particularly perplexing is the observation that bare spin–orbit coupling is far too small to produce the observed polarizations on its own, especially in light-element chiral materials. Often the polarization's dependence on temperature and bias is used as a mechanistic probe.[6–8, 13]

Every CISS observable (spin polarization, magnetoresistance, spin-to-charge conversion) is odd under time reversal and vanishes in thermal equilibrium. A steady signal therefore requires the system to be driven out of equilibrium, and the size and sign of the response are controlled by whatever does the driving. Vibrations have been proposed as one such driver, since a lattice mode can produce an effective, spin-dependent exchange splitting through the spin–orbit coupling.[14] In Ref. [15] we organize competing CISS proposals under a single nonequilibrium selection rule and compare them on one Hamiltonian. That study covers more than vibrations: it also maps orbital-to-spin conversion, length and temperature trends, and the inverse (spin-to-charge) effect. Among the vibrational treatments considered there (coherent and incoherent drives, and quantum baths with and without memory), a

coherent chiral phonon gives by far the largest, most robust polarization. A coherent chiral phonon is a travelling lattice wave of definite wavevector q whose ionic motion circulates and breaks time reversal on its own. Chiral phonons of this kind are now measured directly by circularly polarized Raman scattering, resonant inelastic X-ray scattering, and ultrafast probes,[16–21] and they carry a well-defined angular momentum.[22, 23] Related magneto-chiral terahertz dynamics in photoexcited tellurium have also been reported;[24] we return to that connection elsewhere.

A coherent chiral phonon, however, has a definite wavevector q, and for this effect to be manifest, something must cause its population to dominate over its mirror partner. In thermal equilibrium the $+q$ and $-q$ modes of a nonmagnetic crystal are degenerate time-reversal partners and equally occupied, so the lattice supplies *no* net helicity and cannot, by itself, drive CISS. Something must select one helicity over the other. In the small number of experiments performed under circularly polarized or terahertz illumination the light itself can do this,[16, 19, 21, 25] but the overwhelming majority of CISS measurements are ordinary dc transport experiments with no optical pump at all. A current can also induce phonon angular momentum: analytical expressions have been derived for chiral metals with spin–orbit coupling (the phonon Edelstein effect) and for supercurrents in superconductors with spin–orbit coupling.[26, 27] How a current selects a particular helicity in these experiments requires an explanation, which we present here.

We show that the selection is supplied by the transport current itself. A dc bias places the electrons in a nonequilibrium steady state that damps the two helicities unequally. The imbalance in damping rate $\Delta\gamma = \gamma_{+q} - \gamma_{-q}$ is odd in the current, odd under $q \to -q$, and identical to the nonconservative, "current-induced" Berry force that drives vibrational instabilities in current-carrying nanoconductors.[28–32] Closing the phonon kinetics with a rate equation converts $\Delta\gamma$ into a lattice helicity in two regimes (Fig. 1). At small bias a net helicity $H = n_+ - n_-$ appears with no threshold, growing linearly in the current as $V \to 0$, which follows directly from the odd, continuous vanishing of $\Delta\gamma(V)$ at $V = 0$. This channel exists only through the electron-phonon coupling, and vanishes in its absence. It is present at any finite bias, but above a threshold the preferred helicity's net damping turns negative and it self-amplifies into a coherent travelling wave. This is the coherent chiral phonon we previously identified as the strongest vibrational route to CISS. Ref. [15] showed that a coherent, self-sustained regime can produce an anomalously large signal. In this work, the

origin of the coherent wave is derived rather than assumed. We first develop the theory for the model Hamiltonian of Ref. [15] to establish the effect, and also show that the current-induced asymmetry emerges in a quasi-*ab initio* study of elemental tellurium, with electronic structure, phonons, and their mutual coupling computed from first principles. The effect is specific to chiral systems with finite-q chiral phonons; ordinary achiral conductors show none of it. In all these calculations, Onsager reciprocity is preserved at low bias.

II. MODEL

We use a helical tight-binding wire of the Guo–Sun form [33, 34]: the minimal ingredients needed for a chiral conductor. Sites sit on a helix, each carrying a spin-1/2 orbital. The static Hamiltonian H_0 has three physical ingredients: a uniform on-site energy ε_n, structureless by itself; a nearest-neighbor hopping t; and a chiral spin–orbit coupling of strength $\lambda_{\rm soc}$, built from the local torsion of the backbone,

$$H_0 = \sum_n \varepsilon_n\, c_n^\dagger c_n - t \sum_n \big(c_{n+1}^\dagger c_n + \text{h.c.}\big) + H_{\rm soc},$$
$$H_{\rm soc} = i\lambda_{\rm soc} \sum_n c_{n+2}^\dagger \left(\boldsymbol{\sigma}\cdot\boldsymbol{\nu}_n\right) c_n + \text{h.c.}, \quad \boldsymbol{\nu}_n = \frac{\boldsymbol{a}_n \times \boldsymbol{a}_{n+1}}{|\boldsymbol{a}_n \times \boldsymbol{a}_{n+1}|},$$

with $\boldsymbol{a}_n$ the bond vectors and $\boldsymbol{\sigma}$ the vector of Pauli matrices. Only $H_{\rm soc}$ ties the electron's spin to the sense of the helix; it is the only place chirality enters the electronic Hamiltonian. Two wide-band leads, held at chemical potentials $\mu_{L,R} = \mu \pm eV/2$, drive a steady current through the wire.

A phonon of wavevector q modulates the bonds with a travelling phase e^{iqn} and couples to the electrons through a matrix A_q, giving the full electron–phonon Hamiltonian

$$\mathcal{H} = H_0 + \hbar\omega_0\big(b_q^\dagger b_q + b_{-q}^\dagger b_{-q}\big) + \sum_{Q=\pm q} \big(c^\dagger A_Q c\, b_Q + \text{h.c.}\big). \tag{1}$$

Here $b_Q^\dagger$ creates one quantum of the harmonic phonon mode at wavevector $Q = \pm q$ and bare frequency ω_0. Like H_0, the vertex A_q can have up to three channels: a Holstein term (on-site energy modulation), a hopping modulation, and a modulation of the chiral spin–orbit bond, the only one of the three built from the same chirality vector $\boldsymbol{\nu}_n$ as H_0. The calculations below keep the hopping and chiral spin–orbit channels active and switch the Holstein channel off; the two active channels are comparable in size and interfere, so neither alone stands in for A_q.

The key property of A_q is that it is not Hermitian. Because the travelling phase propagates in one direction along the bonds, $A_{-q} = A_q^\dagger \neq A_q$: the vertex for the $-q$ helicity is the Hermitian conjugate of, not equal to, the vertex for $+q$. This lets the electron bath tell the two helicities apart, once driven. The full Hamiltonian of Eq. (1), vertex and phonon bath included, is Hermitian by construction: every term appears together with its own h.c. partner. H_0 alone, and H_0 plus the phonon coupling with no leads attached at all, are both Hermitian and time-reversal symmetric at every bias.

For Hermitian Hamiltonians, Eq. (3) given below must hold. As a numerical check we find it does so to machine precision in every calculation we ran. The only non-Hermitian object anywhere in this work is the ordinary lead broadening $-\frac{i}{2}(\Gamma_L + \Gamma_R)$: real particle exchange with two reservoirs, external to the Hamiltonian. The current enters through a differential in the leads' chemical potentials, and the effect emerges from the open boundaries under bias.

The electron-induced damping of mode q is read from the electron–phonon self-energy evaluated on the driven Green's functions. Formally, Π_q is the standard one-loop (Migdal) self-energy of the phonon propagator: an electron loop dressed by two insertions of A_q (see Supplemental materials). Because the internal propagators are those of the driven, nonequilibrium steady state, Π_q is purely electronic in origin; the harmonic term in Eq. (1) carries no phonon–phonon interaction of its own. The intrinsic (phonon–phonon) lattice damping is therefore a separate, phenomenological ingredient, $\gamma_{\rm lat}$, added only in the rate-equation closure below. With the greater and lesser phonon self-energies $\Pi_q^{\gtrless}$,

$$\gamma_q^e = \mathrm{Re}\big\{ i\big[\Pi_q^{>}(\omega_0) - \Pi_q^{<}(\omega_0)\big]\big\}\,, \tag{2}$$

with $\gamma_q^e > 0$ damping and $\gamma_q^e < 0$ antidamping. We always write γ_q^e, not the bare γ_q, to flag that this is the *electronic* contribution to a mode's linewidth: the same quantity as $\gamma_\pm^e$ in the rate equation below, and distinct from $\gamma_{\rm lat}$. Equation (2) is simply the Migdal phonon linewidth generalized to a biased steady state. Its two terms are the golden-rule absorption and emission rates, $\Gamma_q^{\rm abs} \equiv \mathrm{Re}\{i\Pi_q^{>}(\omega_0)\}$ and $\Gamma_q^{\rm em} \equiv \mathrm{Re}\{i\Pi_q^{<}(\omega_0)\}$, so that $\gamma_q^e = \Gamma_q^{\rm abs} - \Gamma_q^{\rm em}$. At equilibrium detailed balance forces $\Gamma_q^{\rm abs} > \Gamma_q^{\rm em}$ for every mode. A bias skews the occupation of the electron bath feeding these golden-rule rates; for the helicity whose vertex is preferentially aligned with the current-carrying electrons, $\Gamma_q^{\rm em}$ can grow past $\Gamma_q^{\rm abs}$, flipping the sign of γ_q^e. The inversion lives in the electron bath's occupation, not in an

inverted phonon population.

The symmetry content of this needs no calculation. Time reversal $\mathcal{T}$ reverses the helicity, $\mathcal{T} : q \to -q$, and maps the equilibrium electronic state onto itself. At $V = 0$, therefore,

$$\gamma_{+q}(0) = \gamma_{-q}(0), \tag{3}$$

an exact degeneracy we confirm numerically to machine precision. A bias breaks $\mathcal{T}$ in the electron bath: reversing V is equivalent to a time reversal, so the splitting is odd in V; relabelling $+q \leftrightarrow -q$ at fixed bath is also a time reversal, so the splitting is odd in q too. The physical selection signal is therefore the bias-antisymmetric part

$$\Delta\gamma(V) \equiv \gamma_{+q}(V) - \gamma_{-q}(V) = -\Delta\gamma(-V), \tag{4}$$

which vanishes identically in equilibrium and grows with the current.

III. RESULTS

Helicity-asymmetric damping is the Berry force

Figure 2(a) shows the two dampings as the bias is swept. They coincide at $V = 0$, split under bias, and the softer helicity (the one whose motion is aided by the current) is driven toward antidamping; its γ_q^e crosses zero at a bias we call V_c, defined here in the idealized limit $\gamma_{\rm lat} = 0$. The rate-equation closure below generalizes V_c to the bias where the *total* damping, $\gamma_q^e + \gamma_{\rm lat}$, first crosses zero: a finite lattice damping raises V_c, and removes the instability altogether once $\gamma_{\rm lat}$ exceeds the maximum electronic antidamping $\Delta_{\rm max}$. The difference $\Delta\gamma(V)$ constructed from the standing-wave/circular vertices [Fig. 2(b)] is odd in V, as required by Eq. (4), and rises to a magnitude comparable to the equilibrium damping itself. (Panel (a) uses the traveling-wave vertex of the rate-equation closure; both constructions are odd in V and vanish at equilibrium.)

We now identify $\Delta\gamma$ with a quantity from a different literature. In a real (standing-wave) basis the electronic friction felt by the phonon coordinates is a matrix; a current makes it non-symmetric, and its antisymmetric part is a nonconservative force that does net work around a cycle of the ionic coordinates. This "current-induced" or Berry force is the origin of current-driven vibrational runaway in atomic wires.[28–32] Transforming the two

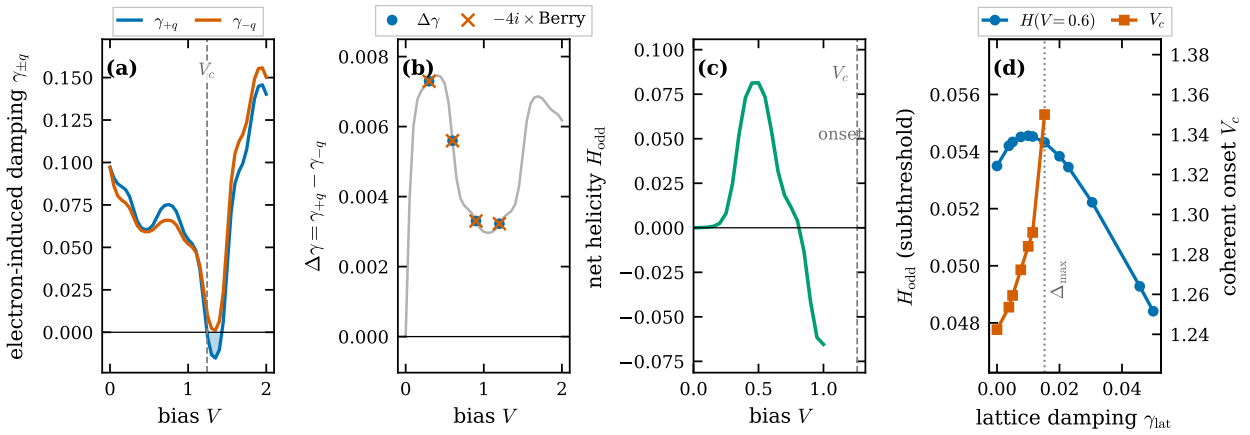


FIG. 2. Helical-wire model. (a) Electron-induced damping of the two helicities versus bias. They are equal at $V = 0$ by time-reversal symmetry and split under bias; the soft helicity is driven toward antidamping and crosses zero at V_c (shaded region: $\min\gamma < 0$). (b) Helicity asymmetry $\Delta\gamma(V)$ from the standing-wave/circular construction (grey line), shown for $V \geq 0$. Circles are $\Delta\gamma$ at selected biases; crosses are the independently computed nonconservative Berry force in the standing-wave basis ($-4i\times$Berry). Circles and crosses fall on the grey line to numerical precision [Eq. (5)]. $\Delta\gamma$ is odd under $V \to -V$, so the negative-bias half is the mirror image (not plotted); panel (a) uses the traveling-wave vertex of the rate-equation closure. (c) Net helicity $H_{\rm odd}$ from the phonon rate equation in the subthreshold window. A finite helicity appears with no threshold; near $V = 0$ it grows linearly with the current, then softens (and can change sign) as V approaches V_c, where the coherent mode takes over. (d) Phase boundary versus intrinsic lattice damping $\gamma_{\rm lat}$: the subthreshold helicity $H_{\rm odd}$ (left axis) is finite for every $\gamma_{\rm lat}$, while a hard coherent onset V_c (right axis) exists only for $\gamma_{\rm lat}$ below the maximum electronic antidamping $\Delta_{\rm max}$.

degenerate standing modes into circular (helicity) combinations, the antisymmetric friction becomes exactly the difference of the two circular dampings. We evaluate the Berry force independently in the standing-wave basis and find

$$\Delta\gamma = -4i \times (\text{Berry force}), \tag{5}$$

holding to the full numerical precision at every bias we checked [symbols and crosses in Fig. 2(b) are indistinguishable]. Both sides of Eq. (5) are two ways of evaluating the same electronic friction matrix $\mathrm{Im}\,\Pi$, in two different bases of the same two-dimensional phonon coordinate (circular for $\Delta\gamma$, standing-wave for the Berry force); Eq. (5) is therefore an

identity between two representations of one object. The three descriptions in circulation (helicity-asymmetric phonon damping, the nonconservative Berry force, and current-induced phonon angular-momentum pumping) are one object computed three ways. Nonconservative current-induced forces are familiar in nanoconductors with more than one vibrational coordinate;[28–32] what is special here is that, in a chiral system, those coordinates are the two circular polarizations of a phonon, so the force becomes a helicity selector.

Six independent checks fix the physical content of $\Delta\gamma$. It vanishes at $V = 0$ [Eq. (3)]; it is nonzero and grows under bias; it is odd in V and odd in q; it is *unchanged* when the helix is mirrored at fixed laboratory q, so the helicity that the current selects is locked to the current and not to the structural handedness; and it is identically zero for an achiral (straight) wire with ordinary Rashba coupling, which carries a current but has no chirality to select. The last two points are the crux of the experimental phenomenology. Handedness does enter CISS, but through a different channel: it sets the axial spin S_z that the selected phonon imprints, and S_z flips under the same mirror that leaves $\Delta\gamma$ invariant. The observed dependence of CISS on both bias polarity and molecular handedness is the product of these two independent sign locks (Fig. 1).

From damping to a lattice helicity

An asymmetry in the damping rates is not yet a population imbalance. To turn $\Delta\gamma$ into a physical helicity we close the phonon kinetics. Each mode exchanges energy with the electrons at the rates contained in Eq. (2) and, in addition, relaxes toward its thermal value $n_B(\omega_0)$ through the intrinsic anharmonic (lattice) damping $\gamma_{\rm lat}$ that any real crystal has. The occupation of each helicity then obeys

$$\frac{dn_\pm}{dt} = \Gamma^{\rm em}_\pm - \gamma^e_\pm\, n_\pm - \gamma_{\rm lat}\big(n_\pm - n_B\big), \tag{6}$$

where $\Gamma^{\rm em}_\pm$ is the electronic emission rate into the mode (the lesser self-energy) and $\gamma^e_\pm$ is the net electronic damping of Eq. (2). In the stable regime, where $\gamma^e_\pm + \gamma_{\rm lat} > 0$, the steady occupations are

$$n_\pm = \frac{\Gamma^{\rm em}_\pm + \gamma_{\rm lat}\, n_B}{\gamma^e_\pm + \gamma_{\rm lat}}. \tag{7}$$

At $V = 0$ the fluctuation–dissipation relation ties emission to damping, $\Gamma^{\rm em}_\pm = n_B\,\gamma^e_\pm$, and Eq. (7) collapses to $n_+ = n_- = n_B$ for *any* $\gamma_{\rm lat}$: no bias, no helicity. Under bias the

numerator and denominator split between the two helicities and a net lattice helicity

$$H = n_+ - n_- \tag{8}$$

develops. A finite open wire carries a small bias-even background from its leads; since the physical selection is odd in the current we report the projection $H_{\rm odd}(V) = \frac{1}{2}[H(V) - H(-V)]$, which isolates it.

Two regimes emerge, and they are physically distinct.

(i) Subthreshold: linear, threshold-free selection. For any bias below V_c, $H_{\rm odd}$ is nonzero and, at small bias, linear in the current [Fig. 2(c)]. There is no threshold: an infinitesimal current already tilts the balance toward one helicity, because $\Delta\gamma$ itself is already nonzero at any finite V (above), and it is only the existence of a coherent, self-sustained mode, not the underlying selection, that requires crossing V_c. We characterize it by a linear susceptibility $\chi_{\rm PE} = dH_{\rm odd}/dV|_{V\to 0}$, which is finite and of order 2×10^{-3} per unit bias in the model.

(ii) Coherent onset. As $V \to V_c$ the net damping of the soft helicity, $\gamma_+^e + \gamma_{\rm lat}$, approaches zero and the linear occupation (7) diverges. Beyond V_c that mode is antidamped and its amplitude grows until anharmonicity limits it. The soft helicity then forms a large-amplitude, definite-q travelling wave generated by the current and not an assumed input, while the competing helicity keeps its ordinary occupation. The coherent regime is the strong-drive limit of the subthreshold current-induced selection.

The boundary between the two regimes is controlled by a single scale, the maximum electronic antidamping $\Delta_{\rm max} = \max_V[-\min(\gamma_{+q}, \gamma_{-q})]$ [Fig. 2(d)]. A hard coherent onset requires the lattice to be soft enough, $\gamma_{\rm lat} < \Delta_{\rm max}$; when the lattice is stiffer than that, the mode never goes unstable and there is no V_c. The subthreshold helicity, in contrast, is robust: for every $\gamma_{\rm lat}$ we tried, $H_{\rm odd}$ at fixed subthreshold bias is nonzero. In a chiral wire the current always chooses a helicity; only the conversion of that choice into a self-sustained coherent wave is conditional on the material's anharmonicity.

Ab-initio validation of the model framework: Tellurium from first principles

The model isolates the mechanism with the minimal set of ingredients. To test whether the same current-induced selection survives in a real material with a real band structure, real spin–orbit coupling, and real chiral phonons, we repeat the construction for elemental

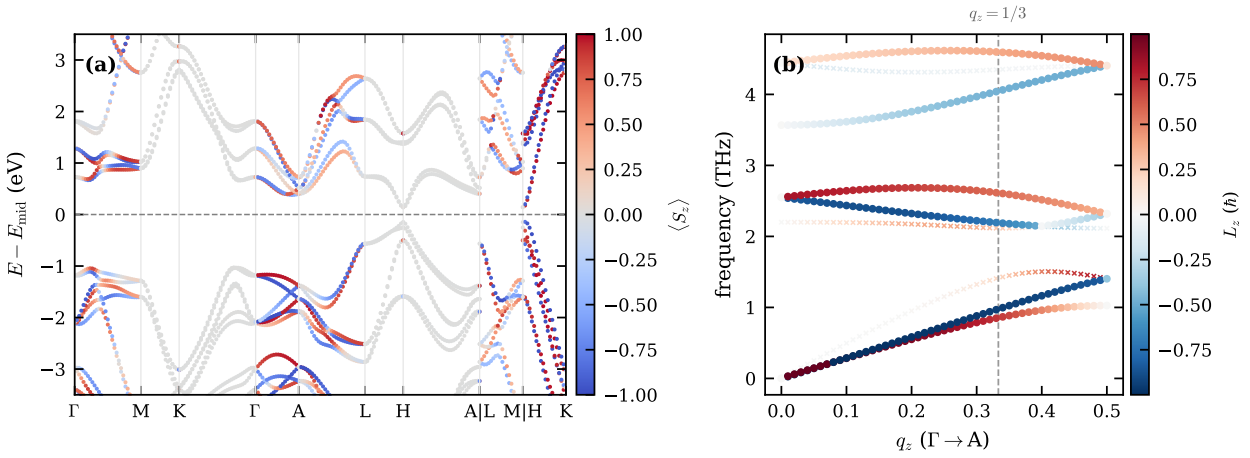


FIG. 3. *Ab initio* ingredients for elemental tellurium. (a) QS$G\hat{W}$+SOC band structure of right-handed tellurium, colored by the spin expectation value $\langle S_z \rangle$; grey marks $\langle S_z \rangle \approx 0$. Computed gap ≈ 285 meV. (b) Chiral phonon dispersion along Γ–A, colored by the on-site angular momentum l_z; filled circles mark the six branches with $|l_z| \gtrsim 0.3$ at $q_z = 1/3$ (dashed line) used in Fig. 4; crosses mark the three that are not. Near $q_z \approx 0.4$ two mid-optical branches cross; an apparent l_z drop on a frequency-sorted index is a branch exchange under that sorting (Supplementary Information).

tellurium. The electronic structure, the phonons, and their mutual coupling are computed from first principles. The transport setup is specified by the chemical potential, the transverse momenta, the number of cells in the wire, the temperature and the lead coupling in the wide-band limit (Methods). At the H point and $V = 0.2$ eV, $\Delta\gamma_{\mathrm{odd}}$ changes by a factor of about 2.6 when the lead coupling is varied from 0.1 to 0.6 eV, and keeps its sign.

Tellurium is the canonical elemental chiral crystal: helical chains of atoms wind around screw axes in space group $P3_121$ (or its enantiomer $P3_221$), it shows a radial spin texture, current-induced bulk magnetization, and chirality-dependent charge-to-spin conversion.[35–37] Our electronic Hamiltonian is constructed from the vertex-corrected quasiparticle self-consistent *GW* (QS$G\hat{W}$) bands including spin–orbit coupling.[38–41] It differs from standard *GW* in that the potential is calculated self-consistently, and it also carries the electron–hole ladder vertex in both the self-energy and the screened interaction. The combination of these extensions yields a high-fidelity one-electron Hamiltonian, shown to be accurate for hundreds of insulators.[42] The computed gap is ≈ 285 meV. The only reported gap [43] is a magneto-optical absorption (excitonic) feature, which probes optical rather than quasiparticle excitations.

The electron–phonon interaction is calculated by the frozen-phonon approach, which requires the change in the electronic Hamiltonian for a nuclear displacement. Generating the full QS$G\hat{W}$ self-energy for each displaced geometry is prohibitively expensive, so we use a variant of the Rigid Self-Energy Approximation, which assumes that the self-energy shift relative to DFT, $\Sigma(\boldsymbol{r}, \boldsymbol{r}') - V_{\mathrm{xc}}^{\mathrm{DFT}}$, shifts rigidly with the displacement of the atomic centres (analogous to the rigid-ion approximation in electron–phonon theory), rather than being re-evaluated self-consistently at every perturbed nuclear position.[44] The density and potential are made self-consistent for each displacement $\boldsymbol{u}$, so the main approximation is that the shift in the effective potential is accurately carried by $\Delta(V^{\mathrm{H}} + V_{\mathrm{xc}}^{\mathrm{DFT}})$ from DFT, equivalent to approximating the QS$G\hat{W}$ susceptibility by the DFT one for the purpose of this shift.[45] We map the electronic Hamiltonian to a real-space, maximally localized Wannier basis of 2×9 orbitals;[46, 47] the projection is essentially exact, since Te p orbitals are the only states near E_F. The diagonal part of the electron–phonon self-energy is kept, obtained from the shift in the eigenvalue, $\partial\varepsilon/\partial\boldsymbol{u}$. This places the band ordering and the spin texture on a first-principles footing. The electron–phonon vertices are frozen-phonon deformation potentials $\partial\mathcal{H}/\partial u$ computed in the same Wannier gauge, so the coupling and the bands are mutually consistent; the on-site terms (the diagonal $\partial\varepsilon/\partial u$) are 0.3–0.7 eV/Å in magnitude across the Wannier basis with the full 18×18 coupling matrix for every hopping given in the Supplemental Material. The phonon eigenvectors are taken from force constants on the identical geometry along the Γ–A line of the screw axis.

Two features of the phonons are essential. First, at the zone centre Γ every optical branch has vanishing phonon angular momentum l_z by point-group symmetry, so a Γ-point phonon gives an identically null selection and contributes nothing; the genuinely chiral modes live at finite q_z along Γ–A, where the screw symmetry endows them with a nonzero l_z.[22] Second, the helicity partner of a finite-q_z mode is the mode at $-q_z$, obtained by the same $q \to -q$ operation as in the model. We form a wire by stacking N cells along the screw axis at fixed transverse momentum $\boldsymbol{k}_\perp$ near the H point, where the band edges lie. The phonon wavevector points along Γ–A, so it conserves $\boldsymbol{k}_\perp$ and couples electron states at the same $\boldsymbol{k}_\perp$. A bulk observable is a sum over $\boldsymbol{k}_\perp$, and we sample it with 19 points, the H point and rings of 6 and 12 points at distances 0.03 and 0.06 (in units of the reciprocal-lattice vectors) from it; we report the mean over these points. A bias enters through wide-band leads exactly as before, and the helicity dampings $\gamma_{\pm q}$ are again the Migdal bubble on the

driven nonequilibrium Green's functions, with the physical signal the bias-odd part $\Delta\gamma_{\mathrm{odd}}$.

Figure 3 shows the two *ab initio* ingredients this construction uses directly: the QS$G\hat{W}$+SOC band structure, colored by the spin expectation value $\langle S_z \rangle$ [Fig. 3(a)], from which the wire Hamiltonian and its Wannier-gauge deformation potentials are built; and the chiral Γ–A phonon dispersion, colored by the angular momentum l_z of each branch's eigenvector [Fig. 3(b)], from which the traveling vertex A_q is built. The valence and conduction band edges sit within a few percent of the H point, the pocket the wire is built near, and six of the nine Γ–A branches carry $|l_z| \gtrsim 0.3$ at $q_z = 1/3$ (filled circles) and are used below; the remaining three (crosses) do not. In the left-handed crystal every chiral branch has the opposite l_z, $l_z(\mathrm{left}) = -l_z(\mathrm{right})$ to better than 10^{-8}, as the mirror symmetry requires. The full electronic structure, Wannier construction, frozen-phonon coupling formula, and branch-by-branch l_z table are given in the Supplemental Material.

Figure 4(a) compares the six chiral Γ–A branches at $V = 0.2$ eV. On the branches at 0.97, 2.62, 4.04 and 4.60 THz the current selects the same helicity at every transverse momentum, with $\Delta\gamma_{\mathrm{odd}} < 0$ and a mean between -3.6 and -13.5 μeV. The 0.85 THz branch has the opposite sign ($+4.8$ μeV) and depends strongly on the length of the wire. On the 2.19 THz branch the mean is -1.4 μeV and the sign changes across the transverse momenta, from -3.1 to $+2.2$ μeV. We analyse the 0.97 THz branch ($l_z = -0.94$, $\hbar\omega_0 = 4.0$ meV), which has the largest effect, -13.5 μeV, and is the best converged.

For this branch the dampings γ_{+q} and γ_{-q} are equal at zero bias and split with the current [Fig. 4(b)]. The odd asymmetry is linear in the bias at small bias, $\Delta\gamma_{\mathrm{odd}} = \chi V$ with $\chi = -1.2 \times 10^{-4}$ (a pure number, V in volts, $\Delta\gamma$ in eV), and χ is negative at every transverse momentum [Fig. 4(b)]. At $V = 0.2$ eV, $\Delta\gamma_{\mathrm{odd}}$ at the H point is between -2.1×10^{-5} and -1.4×10^{-5} eV for wires of 12 to 32 cells. The slope changes from -1.3×10^{-4} at 30 K to -1.0×10^{-4} at 300 K. The asymmetry of about 2×10^{-5} eV at 0.2 V follows from the computed deformation potentials of 0.3–0.7 eV/Å.

The kinetics of Eq. (6) needs the lattice damping γ_{lat}. We compute it with phono3py from the third-order force constants of the same machine-learned potential, for this branch at the same wavevector $q_z = 1/3$. It is 93–99 μeV at 116 K and 250–264 μeV at 300 K for two parameter sets of the potential that agree within about 10% from 30 to 300 K. The same calculation gives the zone-centre optical modes of tellurium within about 15% of the measured Raman frequencies and with linewidths of the size measured.[48] With this lattice

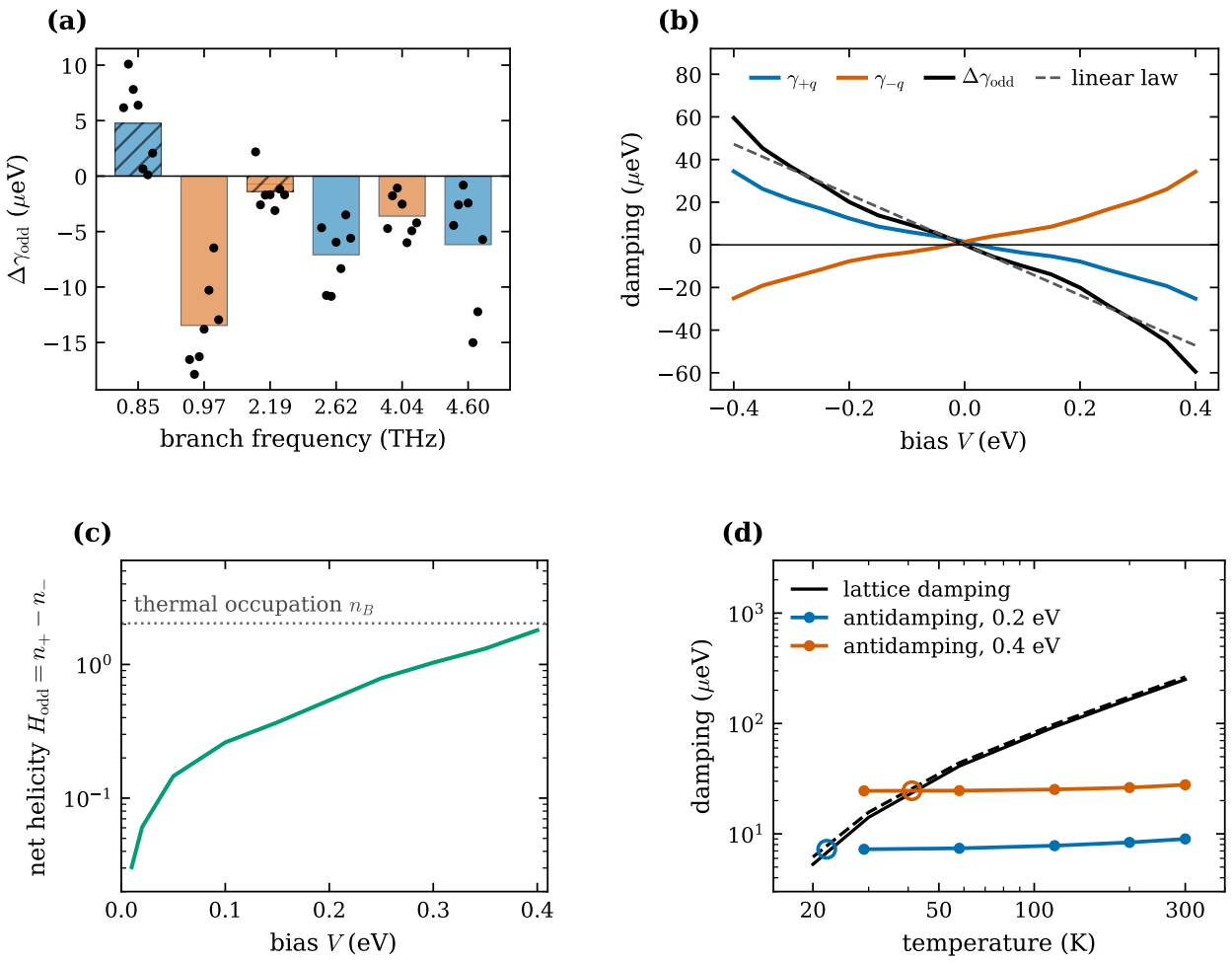


FIG. 4. Elemental tellurium from first-principles electronic structure and phonons. (a) Bias-odd damping asymmetry $\Delta\gamma_{\rm odd}$ at $V = 0.2$ eV for the six chiral Γ–A branches, labelled by frequency and colored by the sign of the phonon angular momentum l_z (blue $l_z > 0$, orange $l_z < 0$); bars show the mean and dots the seven transverse momenta, $N = 16$. Hatched: the 0.85 THz branch depends on the wire length and the 2.19 THz branch changes sign across the transverse momenta. (b)–(d) Branch at 0.97 THz ($l_z = -0.94$), $N = 16$, 116 K unless stated; mean over 19 transverse momenta. (b) Damping of the two helicities, γ_{+q} and γ_{-q}, and the bias-odd asymmetry $\Delta\gamma_{\rm odd}$ versus bias; the dashed line is the linear law fitted for $|V| \leq 20$ meV. (c) Net helicity $H_{\rm odd}$ from the rate equation with the lattice damping from phono3py for two parameter sets of the machine-learned potential (band); the dotted line is the thermal occupation n_B. (d) Lattice damping versus temperature (solid and dashed: the two parameter sets) and the largest electronic antidamping at $V = 0.2$ and 0.4 eV; the coherent regime is reached where the antidamping exceeds the lattice damping, at the crossings marked by open circles (about 22 and 40 K).

damping the current produces a net helicity $H_{\mathrm{odd}} = 0.06$ at 20 mV and 0.5 at 0.2 V, 3% and 26% of the thermal occupation $n_B = 2.0$ of the mode [Fig. 4(c)].

The selection persists to room temperature: at 0.2 V the net helicity is 0.5–0.7 for every temperature from 58 to 300 K. The coherent regime appears when the electronic antidamping exceeds the lattice damping [Fig. 4(d)]. Averaged over the transverse momenta, the antidamping of the favoured helicity is 7–9 μeV at 0.2 V and 25–28 μeV at 0.4 V, nearly independent of temperature, whereas γ_{lat} falls with temperature. The two cross at about 22 K for 0.2 V and about 40 K for 0.4 V, which is 4×10^7 V/m across the 16-cell wire. Above these temperatures the lattice damping exceeds the electronic antidamping at every bias computed, and the helicity takes the finite value given by Eq. (7).

IV. DISCUSSION

We have shown that a biased chiral conductor can populate a chiral phonon without optical pumping, a magnetic field, or a tuned resonance: the charge current selects the helicity. Helicity selection requires structural chirality together with finite-q lattice modes that carry a travelling vertex $A_q \neq A_{-q}$. Ordinary conductors lack that combination: inversion, mirror, or glide symmetries that map $q \to -q$ force $\Delta\gamma \equiv 0$ at any bias, which is why the achiral Rashba wire of Sec. III carries a current with zero helicity selection, and zone-centre modes have $l_z = 0$ by point-group symmetry and give a null. A nonequilibrium steady state is shared by every current-carrying conductor, but which of those conductors convert current into a definite phonon helicity is fixed by Neumann's principle for a time-reversal-odd response tensor. Chirality lifts that symmetry restriction. [49] Onsager reciprocity constrains linear response about thermal equilibrium [50] and is fully respected here: at $V = 0$, time-reversal symmetry enforces $\gamma_{+q} = \gamma_{-q}$, so $\Delta\gamma(0) = 0$ and $H = 0$. A finite bias is itself time-reversal odd, and the response must reverse under $V \to -V$, which Eq. (4) encodes ($\Delta\gamma$ is the bias-antisymmetric part). The leading term $H_{\mathrm{odd}} \propto V$ as $V \to 0$ is the first term of that odd expansion. Above V_c the soft helicity runs away into a coherent amplitude; Eq. (7) diverges smoothly as $V \to V_c^-$, and $\Delta\gamma(V)$ itself stays continuous through the threshold. A phonon-mediated CISS polarization is parallel, while an ordinary electronic Edelstein accumulation is conventionally transverse. (Materials with lower-symmetry spin–orbit coupling can support a longitudinal electronic channel as well, so geometry is a useful

guide rather than a sharp separator.)

The subthreshold helicity is linear and odd in the current, so sweeping V through zero sends $H_{\rm odd}$ continuously through the origin and reverses its sign; at $V = 0$ the system is back in equilibrium with no leftover phonon helicity. What sustains the nonequilibrium state at finite V is the open boundary condition: the leads sit at different chemical potentials, a steady current flows, and energy is exchanged with the reservoirs, while the Hamiltonian remains Hermitian and time-reversal symmetric. Turn the bias off and both the electronic distribution and the phonon helicity relax on ordinary dissipative timescales. Every propagator entering $\Delta\gamma$ is the stationary, time-translation-invariant solution of the driven NEGF equations in the energy domain, so the sign, size, and threshold of the selection are read directly from that steady state. The physical signal is the odd part of H; small even residuals in finite open wires or from approximate electron–phonon vertices are projection artifacts.

Below V_c, the lattice helicity is linear in bias at small V ($H_{\rm odd} \propto V$ from Eq. (7)). Fitting $\Delta\gamma(V) = aV + cV^3$ over the subthreshold window gives a clear negative cubic coefficient: $|cV^3|$ becomes comparable to $|aV|$ well before V_c, so the damping asymmetry softens with bias while remaining odd in V by time reversal. That same odd-in-current structure is what most CISS magnetoresistance measurements report at modest bias.[7, 51] (Higher harmonics of a measured magnetocurrent can also track the lead model.[52]) Only the coherent regime has a threshold.

Three signatures follow. Reversing the current reverses the selected helicity and any phonon-linked spin signal. Reversing the enantiomer reverses the axial spin that spin–orbit coupling attaches to the selected phonon, while the laboratory helicity at fixed q stays put, so the CISS polarization flips with handedness. An achiral conductor shows no selection at any bias. These map directly onto Fig. 1.

Identifying $\Delta\gamma$ with the current-induced Berry force connects the effect to nonconservative forces and current-driven vibrational instabilities in nanoscale conductors;[28–32] in a chiral conductor the coupled coordinates are the two circular polarizations of a phonon, so the force selects helicity, and its strong-drive limit is a coherent chiral phonon. The same reading connects our result to the phonon Edelstein effect[26, 27] and the phonon rotoelectric effect,[53, 54] which describe current- and temperature-driven phonon angular momentum; the subthreshold regime here is the transport member of that family, evaluated on a driven electronic steady state. Converting the selected helicity into a spin polarization

or magnetoresistance requires one further step, the imprint of the selected phonon on the driven electrons, which is treated for the model in Ref. [15].

The phonon Einstein–de Haas effect is related but distinct. The standard definition of phonon angular momentum, $l_\sigma(k) = \hbar\,\epsilon^\dagger_\sigma(k) M \epsilon_\sigma(k)$ with M the generator of rotations about the chiral axis,[22] is exactly the on-site circular ionic motion of mode (k, σ); time reversal enforces $l_\sigma(k) = -l_\sigma(-k)$, so this quantity, like $\Delta\gamma$ in this work, vanishes at equilibrium. A temperature gradient unbalances it in nonmagnetic chiral crystals,[53] and this phonon Einstein–de Haas effect has now been measured directly in single-crystal tellurium as a mechanical torque that reverses with gradient direction and enantiomer.[55] The tellurium branches highlighted in our results have large $|l_z|$ because they are the material's chiral modes at finite q_z. Related work computes the mechanical torque that follows from the current-induced selection established here in tellurium's chiral modes, the electrical analog of the measured thermal Einstein–de Haas torque. [56]

V. CONCLUSIONS

In this paper we establish that a dc electric current selects the helicity of a chiral phonon in a chiral conductor. The bias-antisymmetric damping $\Delta\gamma$ is the nonconservative Berry force on the phonon coordinate; with a phonon rate equation it produces a net lattice helicity at any finite bias and, above a threshold, a self-sustained coherent mode of definite q. That closes the missing step for the coherent-phonon route to CISS that we identified in Ref. [15]: in that work a coherent mode was taken as an assumption; here it is a byproduct of the theory. A quasi-*ab initio* study of elemental tellurium with QS$G\hat{W}$ for the electronic structure shows the same selection for finite-q chiral modes. In tellurium the selection persists from 30 K to room temperature, and the coherent regime appears below about 40 K at the largest bias computed (0.4 V across a 9.5 nm wire). This work determines, for a given band filling and branch, which helicity is populated, and the sign of the selection follows the current. Reversing the bias reverses the selected helicity and any phonon-linked spin signal.

VI. METHODS

Helical-wire model

Figure 2 uses a helical wire of $N = 12$ sites (validation runs use $N = 8$) with unit nearest-neighbor hopping $t = 1$ (the energy unit), chiral spin–orbit strength $\lambda_{\rm soc} = 0.4$, and a chiral phonon of wavevector $q = 2\pi/5$ and frequency $\omega_0 = 0.15$. The electron–phonon vertex keeps the hopping-modulation ($t_1 = 1$) and chiral spin–orbit-modulation ($\lambda_1 = 0.6$) channels active and switches the Holstein (on-site) channel off ($\epsilon_1 = 0$). The two active channels are comparable in magnitude and interfere with each other, so both are needed to evaluate A_q correctly. The electronic part is solved in a wide-band nonequilibrium Green's function scheme[57–59] at temperature $k_BT = 0.02$. The lead self-energies $\Gamma_{L,R}$ are fixed, bias-independent broadenings; bias enters only through the two reservoirs' Fermi functions, so at $V = 0$ ($\mu_L = \mu_R$) they coincide and the Meir–Wingreen current is exactly antisymmetric under exchanging $L \leftrightarrow R$, vanishing identically rather than by cancellation of a small residual. We confirm $I(V{=}0) = 0$ to machine precision in every calculation reported here, despite the leads being the only non-Hermitian part of the problem. The phonon self-energies of Eq. (2) are evaluated on the driven $G^{\gtrless}(E)$ with the energy grid locked to ω_0 so that the shift $E \pm \omega_0$ is exact on the grid.[60] For these parameters the equilibrium damping is $\gamma^e(0) \approx 0.10$, the soft helicity reaches antidamping with $\Delta_{\rm max} \approx 1.5 \times 10^{-2}$ near $V \approx 1.35$, and the electronic instability sits at $V_c \approx 1.24$. The rate equation (6) uses a representative lattice damping $\gamma_{\rm lat} = 5 \times 10^{-3}$ for Fig. 2(c); the phase boundary of Fig. 2(d) sweeps $\gamma_{\rm lat}$ across $\Delta_{\rm max}$. The Berry force of Eq. (5) is computed independently as the antisymmetric part of the electronic friction matrix in the standing-wave basis and agrees with $\Delta\gamma$ to the full working precision at every bias.

Tellurium

The electronic structure is a maximally-localized Wannier interpolation of vertex-corrected quasiparticle self-consistent GW (QS$G\hat{W}$) bands with spin–orbit coupling.[38, 39, 41, 46, 47] Electron–phonon vertices are frozen-phonon deformation potentials $\partial\mathcal{H}/\partial u$ in the same gauge. Phonon eigenvectors and frequencies are obtained from force constants on the identical geometry; the chiral modes are taken at finite q_z along Γ–A, and their angular momenta l_z

are evaluated from the eigenvectors. The full electronic structure, the Wannier construction and its gauge-consistency check, the frozen-phonon coupling formula, and the frequency and l_z of every Γ–A branch are given in the Supplemental Material. The transport wire stacks N cells along the screw axis ($N = 16$ for the results shown, $N = 12$ to 32 in the length tests). The transverse momentum is sampled at 19 points, the H point and rings of 6 and 12 points at distances 0.03 and 0.06 from it (in units of the reciprocal-lattice vectors); the small-bias slope of the asymmetry changes by 2% between these 19 points and the 7 points of the first two shells, which are used for the branch comparison. The chemical potential is set 50 meV below the bulk valence-band maximum at each transverse momentum, wide-band leads with coupling $\gamma_0 = 0.3$ eV carry the bias, and $k_BT = 0.01$ eV (116 K) unless stated. A phonon is damped by all electrons, so $\gamma_{\pm q}$ and $\Gamma^{\mathrm{em}}_{\pm}$ are averaged over the transverse momenta before the rate equation is closed. The lead coupling changes the asymmetry by a factor of 2.6 between $\gamma_0 = 0.1$ and 0.6 eV with the same sign ($\Delta\gamma_{\mathrm{odd}} = -8.0$, -16.5, -21.0×10^{-6} eV for $\gamma_0 = 0.1$, 0.3, 0.6 eV at the H point, $V = 0.2$ eV). The lattice damping is the phonon decay rate from phono3py with the machine-learned potential ($3 \times 3 \times 3$ supercell, displacement 0.03 Å, pair cutoff 6 Å, $12 \times 12 \times 12$ q mesh) at $q = (0, 0, 1/3)$, twice the half-width that phono3py reports, for 20, 30, 58, 116, 200 and 300 K. A $18 \times 18 \times 18$ mesh, an 8 Å cutoff or a $4 \times 4 \times 4$ supercell changes it by up to about one third for the two parameter sets used (`omat_pbe` and `mp_pbe_refit_add`). The inputs beyond first principles are the transport parameters stated here.

DATA AVAILABILITY

The electronic-structure and phonon data reported here were produced with standard open-source packages: Questaal,[40] janus-core,[61] phonopy and phono3py.[62, 63] All input and output files will be provided by the corresponding author upon reasonable request.

AUTHOR CONTRIBUTIONS

S.A. conceived the study, developed the GKBA and SCBA codes and the phono3py interface with janus-core, performed the QS$G\hat{W}$ calculations and all other calculations, and wrote the paper. M.v.S. and J.J. contributed software and the writing of the draft.

ACKNOWLEDGMENTS

This work was authored by the National Laboratory of the Rockies for the U.S. Department of Energy (DOE) under Contract No. DE-AC36-08GO28308. Funding for S.A. and M.v.S. was provided by the Computational Chemical Sciences program within the Office of Basic Energy Sciences, U.S. Department of Energy. SA acknowledges the use of the National Energy Research Scientific Computing Center, under Contract No. DE-AC02-05CH11231 using NERSC award BES-ERCAP0021783, and also acknowledges that a portion of the research was performed using computational resources sponsored by the Department of Energy's Office of Energy Efficiency and Renewable Energy and located at the National Laboratory of the Rockies. The views expressed in the article do not necessarily represent the views of the DOE or the U.S. Government. The U.S. Government retains and the publisher, by accepting the article for publication, acknowledges that the U.S. Government retains a nonexclusive, paid-up, irrevocable, worldwide license to publish or reproduce the published form of this work, or allow others to do so, for U.S. Government purposes.

---

[1] K. Ray, S. P. Ananthavel, D. H. Waldeck, and R. Naaman, Asymmetric scattering of polarized electrons by organized organic films of chiral molecules, Science **283**, 814 (1999).

[2] B. Göhler, V. Hamelbeck, T. Z. Markus, M. Kettner, G. F. Hanne, Z. Vager, R. Naaman, and H. Zacharias, Spin selectivity in electron transmission through self-assembled monolayers of double-stranded DNA, Science **331**, 894 (2011).

[3] Z. Xie, T. Z. Markus, S. R. Cohen, Z. Vager, R. Gutierrez, and R. Naaman, Spin specific electron conduction through DNA oligomers, Nano Lett. **11**, 4652 (2011).

[4] R. Naaman and D. H. Waldeck, Chiral-induced spin selectivity effect, J. Phys. Chem. Lett. **3**, 2178 (2012).

[5] R. Naaman, Y. Paltiel, and D. H. Waldeck, Chiral molecules and the electron spin, Nat. Rev. Chem. **3**, 250 (2019).

[6] F. Evers, A. Aharony, N. Bar-Gill, O. Entin-Wohlman, P. Hegedård, O. Hod, P. Jelinek, G. Kamieniarz, M. Lemeshko, K. Michaeli, V. Mujica, R. Naaman, Y. Paltiel, S. Refaely-Abramson, O. Tal, J. Thijssen, M. Thoss, J. M. van Ruitenbeek, L. Venkataraman, D. H.

Waldeck, B. Yan, and L. Kronik, Theory of chirality induced spin selectivity: Progress and challenges, Adv. Mater. **34**, 2106629 (2022).

[7] B. P. Bloom, Y. Paltiel, R. Naaman, and D. H. Waldeck, Chiral induced spin selectivity, Chem. Rev. **124**, 1950 (2024).

[8] M. van Schilfgaarde, S. Acharya, K. Alberi, L. R. Baker, M. C. Beard, K. Belashchenko, J. Fransson, S. Hammes-Schiffer, M. A. Haque, M. F. Islam, A. I. Krylov, X. Li, J. M. Luther, N. T. Maitra, R. Naaman, M. R. Pederson, Y. Ping, Z. Tao, P. M. Theiler, V. Vlcek, D. Waldeck, B. Yan, I. Zutic, B. Peng, and D. Sun, Challenges and Opportunities in Chiral Induced Spin Selectivity, Newton (2026), in press.

[9] K. Michaeli, V. Varade, R. Naaman, and D. H. Waldeck, A new approach towards spintronics—spintronics with no magnets, J. Phys.: Condens. Matter **29**, 103002 (2017).

[10] H. Lu, J. Wang, C. Xiao, X. Pan, X. Chen, R. Brunecky, J. J. Berry, K. Zhu, M. C. Beard, and Z. V. Vardeny, Spin-dependent charge transport through 2D chiral hybrid lead-iodide perovskites, Sci. Adv. **5**, eaay0571 (2019).

[11] Q. Qian, H. Ren, J. Zhou, Z. Wan, J. Zhou, X. Yan, J. Cai, P. Wang, B. Li, Z. Sofer, B. Li, X. Duan, X. Pan, Y. Huang, and X. Duan, Chiral molecular intercalation superlattices, Nature **606**, 902 (2022).

[12] Y. Dong, A. McConnell, M. P. Hautzinger, M. A. Haque, A. H. Comstock, P. M. Theiler, J. M. Luther, P. C. Sercel, D. Sun, and M. C. Beard, Ultrafast inverse chirality-induced spin selectivity observed by THz emission, Science **390**, 595 (2025).

[13] A. Klein, Y. Yeganeh, A. Capua, O. Millo, and R. Naaman, Temperature dependence of chiral-induced spin selectivity, J. Phys. Chem. C **127**, 3400 (2023).

[14] J. Fransson, Vibrational origin of exchange splitting and chiral-induced spin selectivity, Phys. Rev. B **102**, 235416 (2020).

[15] S. Acharya and M. van Schilfgaarde, Chirality-induced spin selectivity as a nonequilibrium effect: a unified test of competing mechanisms (2026), arXiv:2610.05710.

[16] H. Zhu, J. Yi, M.-Y. Li, J. Xiao, L. Zhang, C.-W. Yang, R. A. Kaindl, L.-J. Li, Y. Wang, and X. Zhang, Observation of chiral phonons, Science **359**, 579 (2018).

[17] L. Zhang and Q. Niu, Chiral phonons at high-symmetry points in monolayer hexagonal lattices, Phys. Rev. Lett. **115**, 115502 (2015).

[18] K. Ishito, H. Mao, Y. Kousaka, Y. Togawa, S. Iwasaki, T. Takenobu, and et al., Truly chiral phonons in α-HgS, Nat. Phys. **19**, 35 (2023).

[19] H. Ueda, M. García-Fernández, S. Agrestini, C. P. Romao, J. van den Brink, N. A. Spaldin, K.-J. Zhou, and U. Staub, Chiral phonons in quartz probed by X-rays, Nature **618**, 946 (2023).

[20] S. R. Tauchert, M. Volkov, D. Ehberger, D. Kazenwadel, M. Evers, H. Lange, A. Donges, A. Book, W. Kreuzpaintner, U. Nowak, and P. Baum, Polarized phonons carry angular momentum in ultrafast demagnetization, Nature **602**, 73 (2022).

[21] I. H. Choi, S. G. Jeong, S. Song, S. Park, D. B. Shin, W. S. Choi, and J. S. Lee, Real-time dynamics of angular momentum transfer from spin to acoustic chiral phonon in oxide heterostructures, Nat. Nanotechnol. **19**, 1277 (2024).

[22] L. Zhang and Q. Niu, Angular momentum of phonons and the Einstein–de Haas effect, Phys. Rev. Lett. **112**, 085503 (2014).

[23] D. M. Juraschek and N. A. Spaldin, Orbital magnetic moments of phonons, Phys. Rev. Materials **3**, 064405 (2019).

[24] Y. Huang, N. Abboud, Y. Lv, P. Zhu, A. Murzabekova, C. Lee, E. A. Pappas, D. Petruzzi, J. Y. Yan, D. Chaudhuri, P. Abbamonte, D. P. Shoemaker, R. M. Fernandes, J. Noronha, and F. Mahmood, Dynamic magneto-chiral instability in photoexcited tellurium, Nat. Phys. **22**, 202 (2026).

[25] T. F. Nova, A. Cartella, A. Cantaluppi, M. Först, D. Bossini, R. V. Mikhaylovskiy, A. V. Kimel, R. Merlin, and A. Cavalleri, An effective magnetic field from optically driven phonons, Nat. Phys. **13**, 132 (2017).

[26] T. Yokoyama, Phonon Edelstein effect in chiral metals, Phys. Rev. B **112**, L020406 (2025).

[27] T. Yokoyama, Supercurrent-induced phonon angular momentum, Phys. Rev. B **114**, 024305 (2026).

[28] D. Dundas, E. J. McEniry, and T. N. Todorov, Current-driven atomic waterwheels, Nat. Nanotechnol. **4**, 99 (2009).

[29] T. N. Todorov, D. Dundas, and E. J. McEniry, Nonconservative generalized current-induced forces, Phys. Rev. B **81**, 075416 (2010).

[30] J.-T. Lü, M. Brandbyge, and P. Hegedård, Blowing the fuse: Berry's phase and runaway vibrations in molecular conductors, Nano Lett. **10**, 1657 (2010).

[31] N. Bode, S. V. Kusminskiy, R. Egger, and F. von Oppen, Scattering theory of current-induced forces in mesoscopic systems, Phys. Rev. Lett. **107**, 036804 (2011).

[32] J.-T. Lü, M. Brandbyge, P. Hegedård, T. N. Todorov, and D. Dundas, Current-induced atomic dynamics, instabilities, and Raman signals: Quasiclassical Langevin equation approach, Phys. Rev. B **85**, 245444 (2012).

[33] A.-M. Guo and Q.-f. Sun, Spin-Selective Transport of Electrons in DNA Double Helix, Phys. Rev. Lett. **108**, 218102 (2012).

[34] A.-M. Guo and Q.-F. Sun, Spin-dependent electron transport in protein-like single-helical molecules, Proceedings of the National Academy of Sciences **111**, 11658 (2014).

[35] M. Sakano, M. Hirayama, T. Takahashi, S. Akebi, M. Nakayama, K. Kuroda, K. Taguchi, T. Yoshikawa, K. Miyamoto, T. Okuda, K. Ono, H. Kumigashira, T. Ideue, Y. Iwasa, N. Mitsuishi, K. Ishizaka, S. Shin, T. Miyake, S. Murakami, T. Sasagawa, and T. Kondo, Radial spin texture in elemental tellurium with chiral crystal structure, Phys. Rev. Lett. **124**, 136404 (2020).

[36] T. Furukawa, Y. Shimokawa, K. Kobayashi, and T. Itou, Observation of current-induced bulk magnetization in elemental tellurium, Nat. Commun. **8**, 954 (2017).

[37] F. Calavalle, M. Suárez-Rodríguez, B. Martín-García, A. Johansson, D. C. Vaz, H. Yang, I. V. Maznichenko, S. Ostanin, A. Mateo-Alonso, A. Chuvilin, I. Mertig, M. Gobbi, F. Casanova, and L. E. Hueso, Gate-tuneable and chirality-dependent charge-to-spin conversion in tellurium nanowires, Nat. Mater. **21**, 526 (2022).

[38] M. van Schilfgaarde, T. Kotani, and S. Faleev, Quasiparticle self-consistent *GW* theory, Phys. Rev. Lett. **96**, 226402 (2006).

[39] T. Kotani, M. van Schilfgaarde, and S. V. Faleev, Quasiparticle self-consistent *GW* method: A basis for the independent-particle approximation, Phys. Rev. B **76**, 165106 (2007).

[40] D. Pashov, S. Acharya, W. R. L. Lambrecht, J. Jackson, K. D. Belashchenko, A. Chantis, F. Jamet, and M. van Schilfgaarde, Questaal: A package of electronic structure methods based on the linear muffin-tin orbital technique, Comput. Phys. Commun. **249**, 107065 (2020).

[41] B. Cunningham, M. Grüning, D. Pashov, and M. van Schilfgaarde, QS$G\hat{W}$: Quasiparticle Self-Consistent *GW* with Ladder Diagrams in W, Phys. Rev. B **108**, 165104 (2023).

[42] M. Grossmann, M. Thieme, M. Grunert, and E. Runge, Many-body perturbation theory vs. density functional theory: a systematic benchmark for band gaps of solids, npj Comput Mater

12, 25 (2026).

[43] H. Shinno, R. Yoshizaki, S. Tanaka, T. Doi, and H. Kamimura, Conduction Band Structure of Tellurium, J. Phys. Soc. Jpn. **35**, 525 (1973).

[44] Q. Yin, A. Kutepov, K. Haule, G. Kotliar, S. Y. Savrasov, and W. E. Pickett, Electronic correlation and transport properties of nuclear fuel materials, Phys. Rev. B **84**, 195111 (2011).

[45] S. Acharya, D. Pashov, A. N. Rudenko, M. Rösner, M. van Schilfgaarde, and M. I. Katsnelson, Importance of charge self-consistency in first-principles description of strongly correlated systems, npj Comput. Mater **7**, 208 (2021).

[46] N. Marzari and D. Vanderbilt, Maximally localized generalized Wannier functions for composite energy bands, Phys. Rev. B **56**, 12847 (1997).

[47] A. A. Mostofi, J. R. Yates, G. Pizzi, Y.-S. Lee, I. Souza, D. Vanderbilt, and N. Marzari, An updated version of `wannier90`: A tool for obtaining maximally-localised Wannier functions, Comput. Phys. Commun. **185**, 2309 (2014).

[48] D. Spirito, S. Marras, and B. Martín-García, Lattice dynamics in chiral tellurium by linear and circularly polarized Raman spectroscopy: crystal orientation and handedness, J. Mater. Chem. C **12**, 2544 (2024).

[49] P. Jacquod, R. S. Whitney, J. Meair, and M. Büttiker, Onsager relations in coupled electric, thermoelectric, and spin transport: The tenfold way, Phys. Rev. B **86**, 155118 (2012).

[50] L. Onsager, Reciprocal relations in irreversible processes. I., Phys. Rev. **37**, 405 (1931).

[51] K. H. Huisman, J.-B. M.-Y. Heinisch, and J. M. Thijssen, Chirality-induced spin selectivity (ciss) effect: Magnetocurrent–voltage characteristics with coulomb interactions i, J. Phys. Chem. C **127**, 6900 (2023).

[52] K. H. Huisman, J.-B. M.-Y. Heinisch, and J. M. Thijssen, Ciss effect: Magnetocurrent–voltage characteristics with coulomb interactions. ii, J. Chem. Phys. **158**, 174108 (2023).

[53] M. Hamada, E. Minamitani, M. Hirayama, and S. Murakami, Phonon angular momentum induced by the temperature gradient, Phys. Rev. Lett. **121**, 175301 (2018).

[54] M. Hamada and S. Murakami, Phonon rotoelectric effect, Phys. Rev. B **101**, 144306 (2020).

[55] H. Zhang, N. Peshcherenko, F. Yang, T. Z. Ward, P. Raghuvanshi, L. Lindsay, C. Felser, Y. Zhang, J.-Q. Yan, and H. Miao, Measurement of phonon angular momentum, Nat. Phys. **21**, 1387 (2025).

[56] S. Acharya and M. van Schilfgaarde, Electrical analog of the einstein–de haas torque in a chiral conductor (2026), unpublished.

[57] Y. Meir and N. S. Wingreen, Landauer formula for the current through an interacting electron region, Phys. Rev. Lett. **68**, 2512 (1992).

[58] A.-P. Jauho, N. S. Wingreen, and Y. Meir, Time-dependent transport in interacting and noninteracting resonant-tunneling systems, Phys. Rev. B **50**, 5528 (1994).

[59] H. Haug and A.-P. Jauho, *Quantum Kinetics in Transport and Optics of Semiconductors*, 2nd ed. (Springer, Berlin, 2008).

[60] T. Frederiksen, M. Paulsson, M. Brandbyge, and A.-P. Jauho, Inelastic transport theory from first principles: Methodology and application to nanoscale devices, Phys. Rev. B **75**, 205413 (2007).

[61] E. Kasoar, P. Austin, H. Devereux, K. Harris, D. Mason, J. Wilkins, F. Zanca, and A. M. Elena, janus-core: tools for machine learnt interatomic potentials, Zenodo (2024).

[62] A. Togo and I. Tanaka, First principles phonon calculations in materials science, Scr. Mater. **108**, 1 (2015).

[63] A. Togo, L. Chaput, T. Tadano, and I. Tanaka, Implementation strategies in phonopy and phono3py, J. Phys.: Condens. Matter **35**, 353001 (2023).

Supplementary Files

This is a list of supplementary files associated with this preprint. Click to download.

- supplemental.pdf